RSC Advances

PAPER

View Article Online
View Journal | View Issue

Cite this: *RSC Adv.*, 2017, 7, 24359

Improved rate capability of a $LiNi_{1/3}Co_{1/3}Mn_{1/3}O_2$/CNT/graphene hybrid material for Li-ion batteries

Xing Li, *[a] Xing Zhao,[a] Ming-Shan Wang,[a] Kang-Jia Zhang,[a] Yun Huang,[a]
Mei-Zhen Qu,[b] Zuo-Long Yu,[b] Dong-sheng Geng, *[c] Wen-gao Zhao[d]
and Jian-ming Zheng*[d]

Received 24th March 2017
Accepted 27th April 2017

DOI: 10.1039/c7ra03438e

rsc.li/rsc-advances

In this work, a $LiNi_{1/3}Co_{1/3}Mn_{1/3}O_2$/CNT/Graphene nanosheet (NCM/CNT/GN) hybrid material has been successfully prepared by a facile wet chemical method. The hierarchical structures of the CNT and GN are well maintained in the NCM/CNT/GN hybrid material, and their addition does not affect the layered crystal structure of the NCM. It is found that the NCM/CNT/GN hybrid material forms a three-dimensional (3D) spider-web like network structure *via* the interconnection of one-dimensional CNT and two-dimensional GN. As a result, the NCM/CNT/GN hybrid material exhibits the least electrode polarization, significantly enhanced rate capability with a high discharge capacity of 134 mA h g^{-1} at 3.0C, as well as excellent cycling performance. The improved electrochemical performances of NCM/CNT/GN hybrid material could be well correlated with the synergistic effects of CNT and GN, efficiently building the 3D conductive network, which largely enhances the electronic conductivity and the lithium ion diffusion in the NCM electrode.

Introduction

Lithium-ion batteries (LIBs) as important energy storage devices have been widely used in various electronic devices such as cellular phones, cameras, laptop computers, *etc.* In view of their high energy density and good cyclability, recently LIBs have also regarded as the preferred power sources for hybrid electric vehicle (HEV) or electric vehicle (EV).[1–3] $LiCoO_2$ is one of the most widely used cathode materials in commercial LIBs. However, its drawbacks of high cost, poor thermal stability, toxicity and a low practical specific capacity of 130–140 mA h g^{-1} have fundamentally limited its large-scale application in LIBs dedicated for HEV or EV.[4] To enable vehicle electrification, there is an urgent demand for developing new generation of LIBs with high energy density, high power capability and long cycle life.[5–7] An appropriate selection of the cathode material is one of the key factors in improving the energy density and other performances of LIBs. Recently, a series of layer structured metal oxides of $LiNi_xCo_yMn_zO_2$ have been widely investigated due to their improved structural stability and electrochemical properties as compared to traditional $LiCoO_2$,[8–10] including $LiNi_{1/3}Co_{1/3}Mn_{1/3}O_2$, $LiNi_{0.8}Co_{0.1}Mn_{0.1}O_2$, $LiNi_{0.5}Co_{0.2}Mn_{0.3}O_2$. Among them, $LiNi_{1/3}Co_{1/3}Mn_{1/3}O_2$ has attracted much research attention as one of the mixed transition metal oxides because of its relatively low content of Co, high specific capacity and superior thermal stability.[11]

However, the $LiNi_{1/3}Co_{1/3}Mn_{1/3}O_2$ still suffers from some technical challenges. The first one is the undesired interfacial reactions between $LiNi_{1/3}Co_{1/3}Mn_{1/3}O_2$ and electrolytes, which could be attributed to the catalytic effects of the redox couple of $Co^{3+/4+}$ that is incurred when the $LiNi_{1/3}Co_{1/3}Mn_{1/3}O_2$ is being charged up to a high cut-off voltage of 4.55 V.[12,13] The second one is the structure disruption and cation disorder between Li^+ and Ni^{2+} in the $LiNi_{1/3}Co_{1/3}Mn_{1/3}O_2$ crystal lattice, which can reduce the specific capacity and deteriorate the cycling stability of $LiNi_{1/3}Co_{1/3}Mn_{1/3}O_2$.[14] The third one is the relatively poor electronic conductivity of the $LiNi_{1/3}Co_{1/3}Mn_{1/3}O_2$ resulting in serious electrode polarization and poor rate capability, which limits the practical application of $LiNi_{1/3}Co_{1/3}Mn_{1/3}O_2$ as cathode in the power-type LIBs for HEV or EV.[15] To prevent the interfacial side reactions, researchers have attempted to coat the $LiNi_{1/3}Co_{1/3}Mn_{1/3}O_2$ with chemically stable and electrochemically inert materials such as $FePO_4$,[16] Al_2O_3,[17] $AlPO_4$,[18] *etc.* To decrease the cation disorder, some strategies such as Al partial substitution for Mn[19] or Co;[20] Fe partial substitution for Mn;[21] F[22] partial substitution for O anion, in the $LiNi_{1/3}Co_{1/3}Mn_{1/3}O_2$ crystal lattice, even Ti[23] surface doping have been implemented.

As the poor electronic conductivity of $LiNi_{1/3}Co_{1/3}Mn_{1/3}O_2$ may considerably affects the electrode polarization and thus

---

[a] *The Center of New Energy Materials and Technology, School of Materials Science and Engineering, Southwest Petroleum University, Xindu Road 8, Chengdu 610500, China. E-mail: lixing@swpu.edu.cn; Fax: +86 28 83037409; Tel: +86 28 83037409*

[b] *Chengdu Institute of Organic Chemistry, Chinese Academy of Science, Chengdu 610041, China*

[c] *Center for Green Innovation, School of Mathematics and Physics, University of Science and Technology Beijing, Beijing, 100083, China. E-mail: dgeng@ustb.edu.cn*

[d] *Energy and Environment Directorate, Pacific Northwest National Laboratory, 902 Battelle Boulevard, Richland, WA 99354, USA. E-mail: jianming.zheng@pnnl.gov*

rate capability of LIBs, acetylene black is usually adopted as conductive additive to increase the electronic conductivity and therefore improve electrochemical performance of NCM cathodes, especially the rate capability.[24,25] However, it is difficult to effectively establish an electrical percolation network due to the non-uniform dispersion of nano carbon particles in the mixing procedure.[26,27] Owing to the high electronic conductivity, large specific surface area and excellent structural stability, carbon nanotube (CNT)[28,29] and graphene nanosheet (GN)[30] have been used as conductive nanostructured carbon matrices to improve the electronic conductivity, specific capacity, rate capability and cycling stability of the $LiNi_{1/3}Co_{1/3}Mn_{1/3}O_2$. However, both the CNT and GN are inclined to agglomerate because of the influence of van der Waals force and surface functional groups. Therefore, only CNTs or sole GNs might not be capable of efficiently building a conductive network in the electrode to improve the particle-to-particle electronic transfer of the active material. It is necessary to avoid the self-aggregation while constructing a three-dimensional carbon network by sufficiently utilizing the advantages of one-dimensional (1D) CNT and two-dimensional (2D) GN.

In the present study, we prepared a $LiNi_{1/3}Co_{1/3}Mn_{1/3}O_2$/CNT/GN (short as NCM/CNT/GN) hybrid material that possesses the conductive nanostructured carbon matrix composed of both CNT and GN. In the structure of hybrid material, the 2D graphene nanosheet covered on the surface of isolated NCM particles, while the 1D carbon nanotubes act as bridges to connect the NCM particles and the graphene nanosheets. This synergistic effect of 1D CNTs and 2D GNs efficiently built a three-dimensional (3D) conductive spider-web like framework in the electrode. Taking advantages of the 3D conductive carbon network, the materials exhibited lower electrode polarization, better rate capability and improved cycling stability than those of NCM/CNT or NCM/GN counterparts.

Experimental

Preparation of the layered metal oxide $LiNi_{1/3}Co_{1/3}Mn_{1/3}O_2$

The layered structure lithium metal oxide $LiNi_{1/3}Co_{1/3}Mn_{1/3}O_2$ (NCM) was synthesized by a facile wet chemical method. Firstly, the $Ni(CH_3COO)_2 \cdot 4H_2O$, $Co(CH_3COO)_2 \cdot 4H_2O$, and $Mn(CH_3COO)_2 \cdot 4H_2O$ (mole ratio of Ni : Co : Mn = 1 : 1 : 1) were dissolved in deionized water to form a stable solution. Then, the stoichiometric amount of Li_2CO_3 was slowly added into the above solution to form a uniform mixture. 6% excess of Li source was used to compensate the volatilization loss during calcination at high temperature. The mixture was heated at 373 K with magnetic stirring for 4 h to obtain a brown powder. Finally, the brown powders were calcined at 1073 K for 8 h in air atmosphere to obtain the product of $LiNi_{1/3}Co_{1/3}Mn_{1/3}O_2$.

Preparation of NCM/CNT/GN, NCM/CNT and NCM/GN hybrid materials

For preparation of the NCM/CNT/GN, first, 60 mg of CNT (hydroxyl multi-wall carbon nanotubes, >50 nm in diameter, 5–10 μm in length and >95 wt% in purity, Timesnano) and graphene nanosheet (less than 10 layers, 3–5 μm in diameter, >99 wt% in purity, Daying Juneng Co., Ltd) with a mass ratio of 1 : 2 was dispersed in 30 ml ethanol with ultrasonication to form a stable suspension. Then, 540 mg of $LiNi_{1/3}Co_{1/3}Mn_{1/3}O_2$ (weight ratio of $LiNi_{1/3}Co_{1/3}Mn_{1/3}O_2$ to (CNT + GN) was 90 : 10) was added into the above suspension. Finally, with vigorous magnetic stirring and heating at 353 K to evaporate the ethanol, the black $LiNi_{1/3}Co_{1/3}Mn_{1/3}O_2$/CNT/GN hybrid material with 10 wt% of CNT + GN conductive carbon framework was obtained. The $LiNi_{1/3}Co_{1/3}Mn_{1/3}O_2$/CNT and $LiNi_{1/3}Co_{1/3}Mn_{1/3}O_2$/GN hybrid materials were prepared in a similar manner. The percentage of the CNT or GN in the hybrid was controlled the same at 10 wt%. The $LiNi_{1/3}Co_{1/3}Mn_{1/3}O_2$/acetylene black (NCM/AB) hybrid material with 10 wt% AB was also prepared for comparison.

Materials characterization

The crystallographic information of the hybrid samples was characterized by X-ray powder diffraction (XRD, Xpert MPD DY1219) with a scan speed of $5° \min^{-1}$ in the 2θ range of 10–90°. The morphology features of the as-prepared hybrid materials corresponding electrodes were scrutinized by scanning electron microscopy (SEM, FEI INSPECT-F). The Raman spectra of the hybrid materials were recorded on a Renishaw InVia using laser excitation wavelength of 785 nm.

Electrochemical measurements

The cathode electrode was prepared by coating mixture slurries containing 95 wt% hybrid cathode material and 5 wt% LA-132 binder onto an aluminum foil. The weight of active material containing the conductive nanostructured carbon matrix in the working electrode was about 3.50 mg, and the geometric area of the electrode was 1.54 cm^2. The specific capacity is calculated on the basis of NCM. In an Ar-filled glovebox, the cathode electrode was assembled into R2032 coin-type cell with Li metal as anode electrode and Celgard 2400 as separator. The electrolyte was 1 M $LiPF_6$ in ethylene carbonate (EC), diethyl carbonate (DEC) and dimethyl carbonate (DMC) (EC : DEC : DMC volume ratio of 1 : 1 : 1). The electrochemical performance measurements of the hybrid cathodes were carried out on BTS-5V 20 mA cell testing instrument (NEWARE Electronic Co., Ltd) between cut-off voltages of 2.5–4.6 V (*vs.* Li/Li^+) at different charge/discharge current rates at room temperature. The specific capacity of the hybrid cathode was calculated based on the mass of active $LiNi_{1/3}Co_{1/3}Mn_{1/3}O_2$. The electrochemical impedance spectroscopy (EIS) measurements were performed at charged state of 4.6 V using a CHI660D electrochemical workstation in the frequency range from 100 kHz to 0.01 Hz with a potential perturbation of 5 mV. The cyclic voltammogram (CV) of the hybrid material electrode was recorded between 2.5–4.6 V (*vs.* Li/Li^+) with a scan rate of 0.1 mV s^{-1}.

Results and discussion

The schematic illustration of the preparation process of the NCM/CNT/GN hybrid materials is shown in Fig. 1a. A facile wet chemical method is adopted to construct the 3D conductive nanostructured carbon framework composed of CNT, GN and NCM particles. An appropriate amount ethanol is added as dispersant. Then, the NCM, CNT, and GN are dispersed to form a uniform suspension with the help of ultrasonication. Through the wet chemical method, the NCM, CNT, and GN are homogeneously redistributed by the ethanol dispersant. During the drying process, the isolated materials of NCM, CNT, and GN become interconnected with each other due to the interactions between the NCM particle and the surface functional groups of CNT and GN. The graphene nanosheets are stretched by the NCM particles, and meanwhile the graphene nanosheets closely cover on the surface of NCM particles. Furthermore, the CNTs homogeneously distribute between the gaps of NCM particles and graphene nanosheets, which form a conducting bridge to facilitate the transfer of lithium ions and electrons. The preparation processes of the NCM/GN (Fig. 1b), NCM/CNT (Fig. 1c) and NCM/AB (Fig. 1d) hybrid materials are similar to that of NCM/CNT/GN hybrid material. However, compared with the structure of 3D NCM/CNT/GN, due to the high surface activity and large specific surface area of nano materials, single 0D AB, 1D CNT, or 2D GN as conductive additive all exist severe agglomeration and could not efficiently construct a conductive nanostructured carbon network.

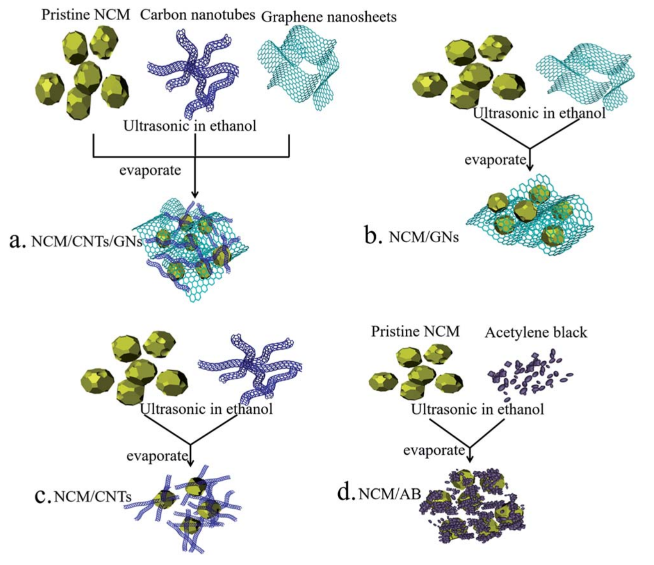

Fig. 1 Schematic illustration of the preparation of NCM/CNT/GN (a), NCM/GN (b), NCM/CNT (c), and NCM/AB (d) hybrid materials.

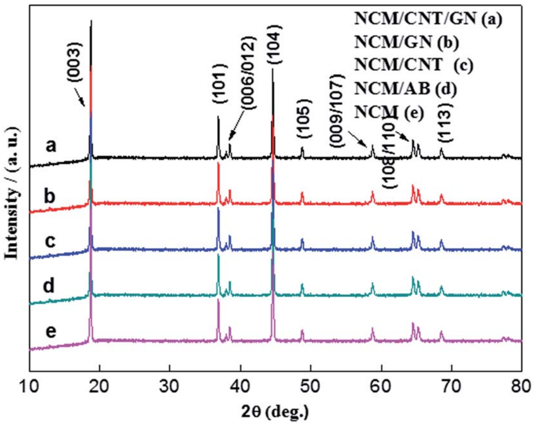

Fig. 2 XRD patterns of the pristine NCM, NCM/AB, NCM/CNT, NCM/GN and NCM/CNT/GN composites.

Table 1 The lattice parameters of NCM/CNT/GN, NCM/GN, NCM/CNT, NCM/AB hybrid materials and the pristine NCM

Samples	a/Å	c/Å	$I_{(003)}/I_{(104)}$
NCM/CNT/GN	2.851	14.299	1.333
NCM/GN	2.853	14.231	1.332
NCM/CNT	2.852	14.230	1.331
NCM/AB	2.850	14.232	1.331
NCM	2.853	14.231	1.332

The XRD patterns of pristine NCM (e), NCM/ABs (d), NCM/CNTs (c), NCM/GNs (b) and NCM/CNT/GN (a) are presented in Fig. 2. It can be found that all samples exhibit similar XRD patterns which can be indexed to α-$NaFeO_2$ type hexagonal structure with a space group $R\bar{3}m$, with no extra impurity peaks being found. The splitting doublets of (006/012) and (108/110) at *ca.* 38° and *ca.* 65° are clearly identified, which indicates that NCM particles in all samples have a well-defined layered structural characteristics.[31,32] The intensity ratio of (003)/(104) is determined to be about 1.331 for all samples, indicating a low Ni^{2+}/Li^{+} cation mixing in the prepared NCM hybrid cathode material. The calculated lattice constants for NCM, NCM/CNT, NCM/AB, NCM/GN and NCM/CNT/GN are compared in Table 1, which are close to each other suggesting that the CNT + GN, GN, CNT or AB do not affect the layered crystal structure of active NCM.

Fig. 3 shows the Raman spectra of NCM/CNT/GN (a), NCM/GN (b), NCM/CNT (c), NCM/AB (d) and pristine NCM (e). It can be clearly observed that the pristine NCM powders displays only two bands of A_{1g} and E_g at about 465 cm^{-1} and 585 cm^{-1} respectively. In the NCM layered structure, the M (transition metal)–O stretching and O–M–O bending of oxygen atom contribute to the A_{1g} and E_g bands.[33] Raman spectra of the

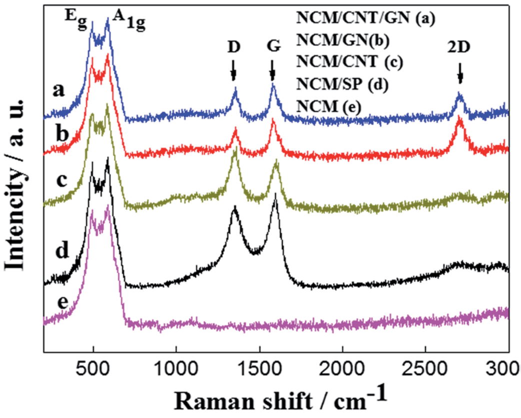

Fig. 3 Raman spectra of the pristine NCM, NCM/AB, NCM/CNT, NCM/GN and NCM/CNT/GN hybrid materials.

NCM/CNT/GN, NCM/GN, NCM/CNT and NCM/AB hybrids show two additional bands at about 1306 and 1593 cm^{-1}, which can be assigned to the D and G bands of graphene, carbon nanotube and acetylene black. The D bands reflect the defect or disorder in the carbon crystals, the G bands arise from the in-plane vibration of sp^2 carbon atoms of graphene sheet.[34,35] The NCM/CNT/GN and NCM/GN show strong 2D bands at about 2700 cm^{-1}, which is the characteristic of graphene nanosheets.[36,37] These results indicate that the structures of CNT + GN, GN, CNT or AB are maintained during the preparation of the hybrid materials.

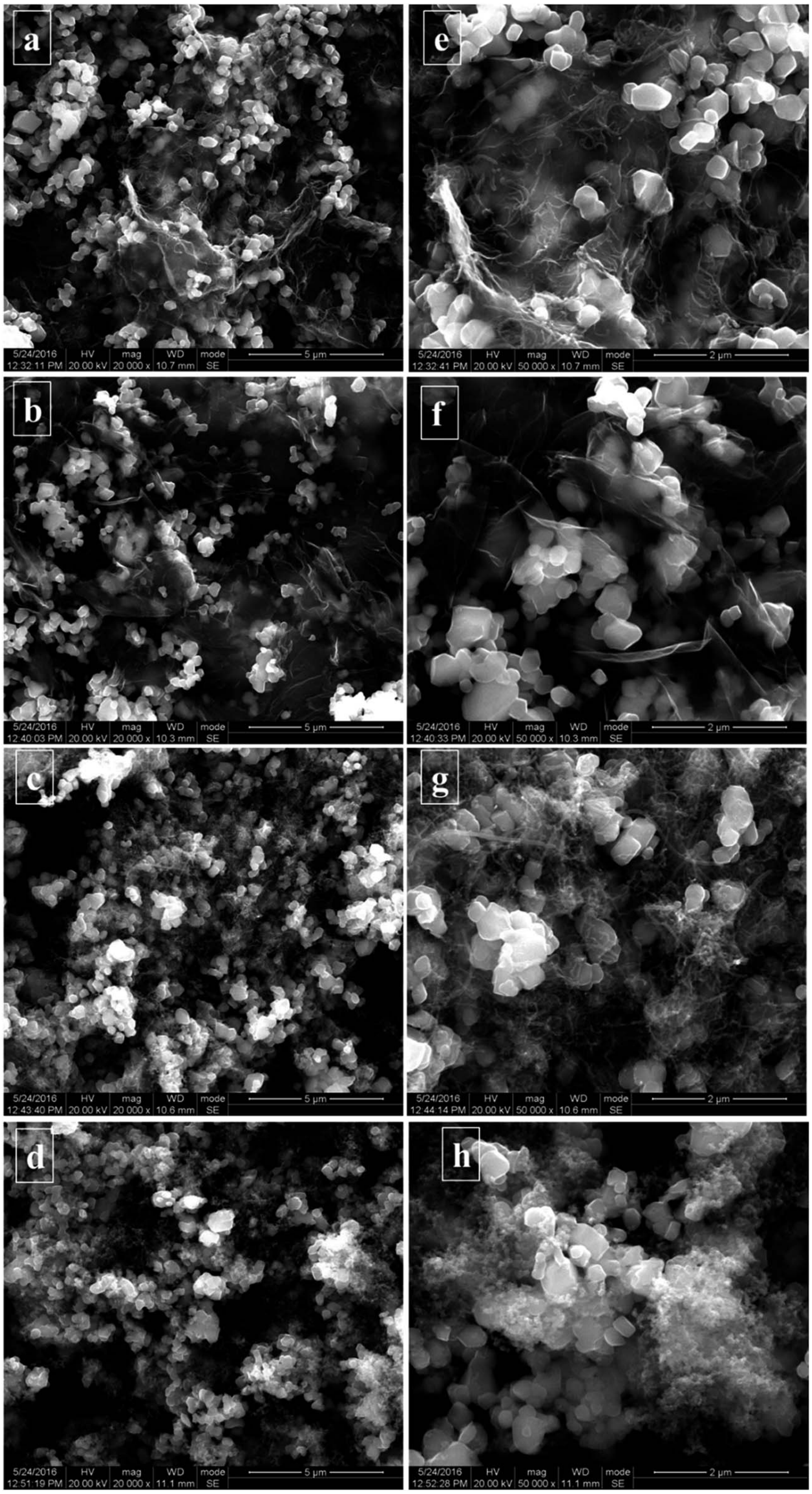

Fig. 4 SEM images of NCM/CNT/GN (a and e), NCM/GN (b and f), NCM/CNT (c and g), and NCM/AB (d and h) electrodes.

The SEM images of NCM/CNT/GN, NCM/GN, NCM/CNT, and NCM/AB electrodes at high magnifications are shown in Fig. 4. As shown in Fig. 4d and h, the NCM material shows polyhedral shape with average particle size ranging from 300 nm to 500 nm. Furthermore, it can be seen that the agglomerated AB barely piles on the surface of some NCM particles, and the most surface of NCM particles are exposed. On the one hand, the exposed surface would lead to the undesired interfacial reactions especially at high voltages. On the other hand, the agglomeration of AB particles also leads to the decrease of the electrical conductivity, which means that the electrochemical rate capability might be compromised. From Fig. 4c and g, as it can be seen, the CNTs are intertwined to form agglomerates that are randomly distributed on the NCM particles. At the same time, there still exists some uncoated surface of the NCM particles. The sample of NCM/GN in the Fig. 4b and f shows that the particles of NCM active material are homogeneously dispersed on the graphene nanosheets, and to some extent, some of graphene nanosheets act as a coating layer to cover and wrap the NCM particles. However, a large number of NCM particles do not directly connect with graphene layer and distributed in the empty space of graphene sheets. Compared with the NCM/CNT, NCM/GN and NCM/AB, the NCM/CNT/GN hybrid material shown in the Fig. 4a and e presents that graphene nanosheets homogeneously dispersed in the electrode, and most of the NCM particles are coated within the graphene nanosheets. Besides, carbon nanotubes are distributed on the graphene sheets and NCM particles, which function as a bridge to construct a 3D spider web like electronic conducting network. Such a unique network structure could largely improve the electronic conductivity of NCM electrode. In addition, it may also mitigate the interfacial reaction between active material and the electrolyte.

Table 2 Potential difference of the redox peaks for NCM/CNT/GN, NCM/GN, NCM/CNT and NCM/AB obtained from the initial CV curves

Samples	Anodic peak (V)	Cathodic peak (V)	Potential difference (V)
NCM/CNT/GN	4.09	3.65	0.44
NCM/GN	4.06	3.60	0.46
NCM/CNT	4.15	3.63	0.52
NCM/AB	4.12	3.52	0.60

The CV curves for the NCM/CNT/GN (a), NCM/GN (b), NCM/CNT (c) and NCM/AB (d) hybrids recorded at a scan rate of 0.1 mV s^{-1} from 2.5 to 4.6 V are demonstrated in Fig. 5. The CV curves show a cathodic peak at about 3.6 V, and an anodic peak at about 4.1 V for all samples. No reduction peak appears at 3.2 V, which is the reduction of Mn^{4+}, indicating that the Mn keeps the oxidation status of +4 in the hybrid material.[38] The well-defined redox peaks indicating the reversible extraction and insertion of lithium ions out of/into the NCM crystal. And those redox peaks are corresponding to the Ni^{2+}/Ni^{4+} and Co$^{3+/4+}$ redox couples.[39,40] As shown in Table 2, it can be observed that the NCM/CNT/GN hybrid material shows the smallest potential

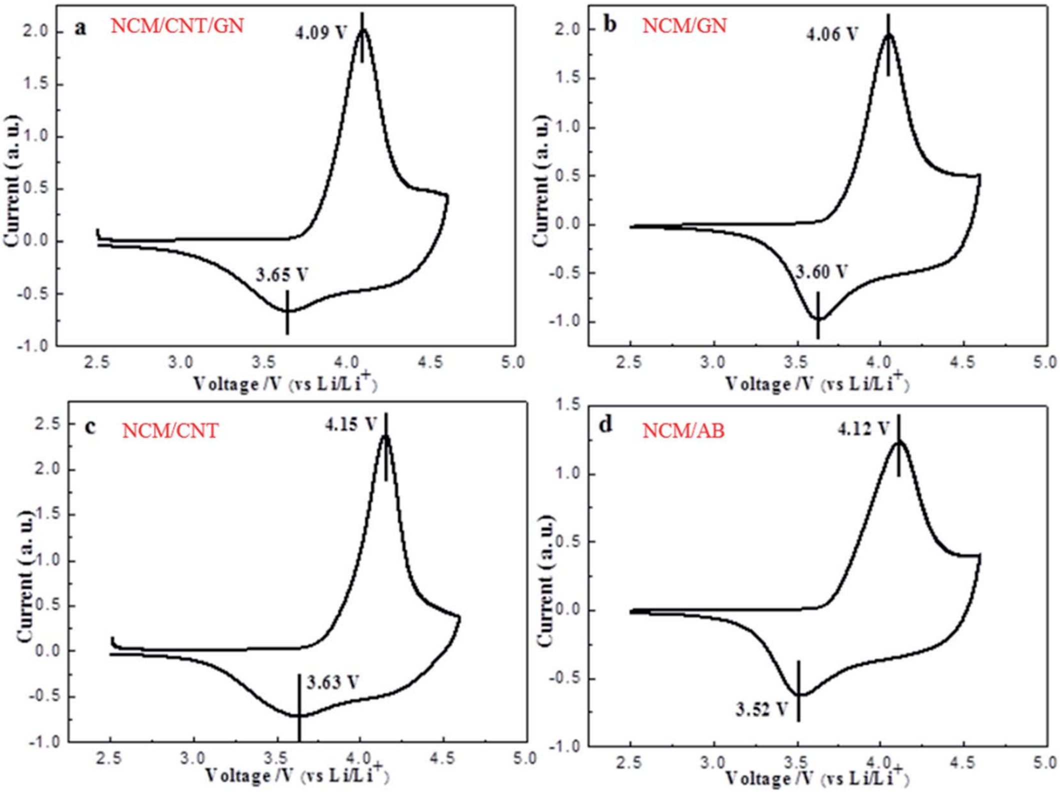

Fig. 5 CV curves of NCM/CNT/GN (a), NCM/GN (b), NCM/CNT (c) and NCM/AB (d) at a scan rate of 0.1 mV s^{-1} from 2.5 to 4.6 V.

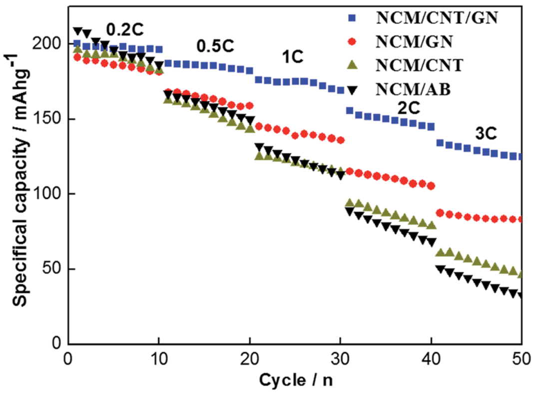

Fig. 6 Rate performances of the NCM/CNT/GN, NCM/GN, NCM/CNT and NCM/AB hybrids in the voltage range of 2.5–4.6 V.

difference between the oxidation and reduction peaks among the samples, which confirms that the lowest electrode polarization can be achieved by the introduction of both GN and CNT. The enhanced electrochemical reaction kinetics could be ascribed to the efficient spider web like conducting network contributed by the synergistic effects of CNT and GN.

Fig. 6 shows the specific discharge capacities of NCM/CNT/GN, NCM/GN, NCM/CNT and NCM/AB electrodes at various current rates. In the voltage range of 2.5–4.6 V (*vs.* Li/Li$^+$), the NCM/CNT/GN, NCM/GN, NCM/CNT, and NCM/AB hybrid materials show the initial discharge capacities of 200 mA h g^{-1}, 191 mA h g^{-1}, 196 mA h g^{-1} and 209 mA h g^{-1} at 0.2C, respectively. Although NCM/CNT/GN hybrid material does not show obvious advantage in the discharge specific capacity at low current rate of 0.2C, it exhibits obviously higher discharge capacities upon increasing current rates, ranging from 0.5 to 3.0C, than those of NCM/GN, NCM/CNT or NCM/AB. The discharge capacities of NCM/CNT/GN at the rates of 0.5C, 1.0C, 2.0C and 3.0C are 187 mA h g^{-1}, 175 mA h g^{-1}, 156 mA h g^{-1} and 134 mA h g^{-1}, respectively. Especially at high rate of 3.0C, the NCM/CNT/GN is still capable of delivering a high specific capacity of 134 mA h g^{-1}, which is much higher than those of NCM/GN (87 mA h g^{-1}), NCM/CNT (62 mA h g^{-1}), and NCM/AB (51 mA h g^{-1}). These could be closely correlated with the efficient increase of electronic conductivity in the presence of the 3D conductive network of CNT and GN, which alleviates the electrode polarization especially at high current rates. The improved rate capability of the NCM/CNT/GN also was reported by using zinc as anode in an neutral Li_2SO_4 solution.[41]

Fig. 7 further compares the charge and discharge curves of the NCM/CNT/GN, NCM/GN, NCM/CNT and NCM/AB hybrids. It can be observed that all the sample exhibit the similar voltage plateaus between 3.5–4.0 V. Obviously, the NCM/CNT/GN hybrid shows the least increase of electrode polarization with the rising of charge/discharge current densities, therefore,

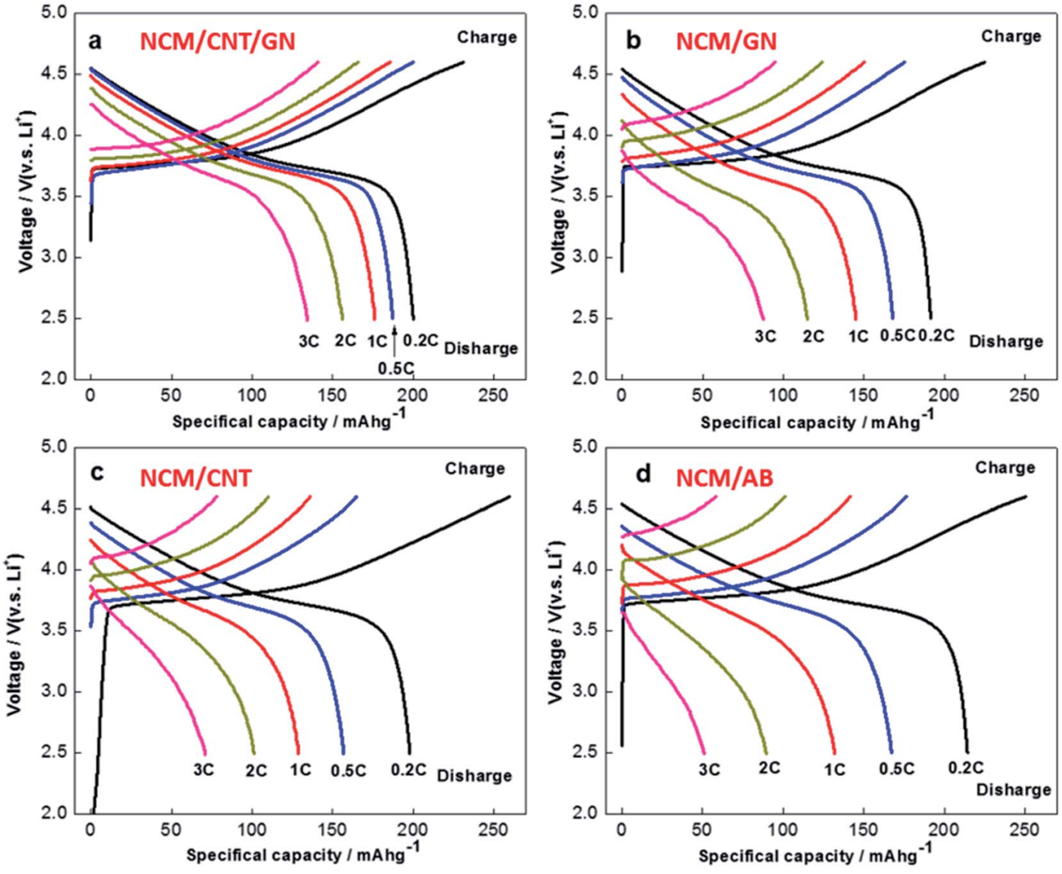

Fig. 7 Charge and discharge curves of the NCM/CNT/GN, NCM/GN, NCM/CNT and NCM/AB hybrids.

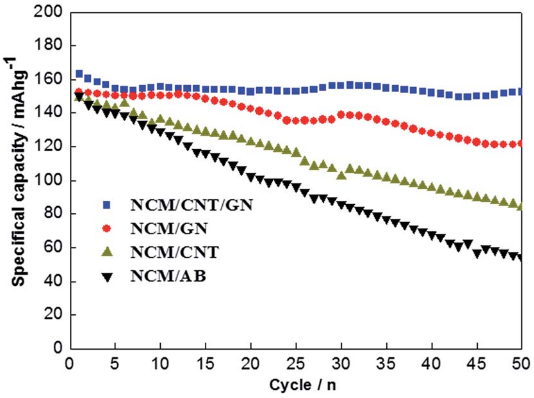

Fig. 8 Cycling performance of the NCM/CNT/GN, NCM/GN, NCM/CNT and NCM/AB hybrids at 1.0C rate in the voltage range of 2.5–4.6 V.

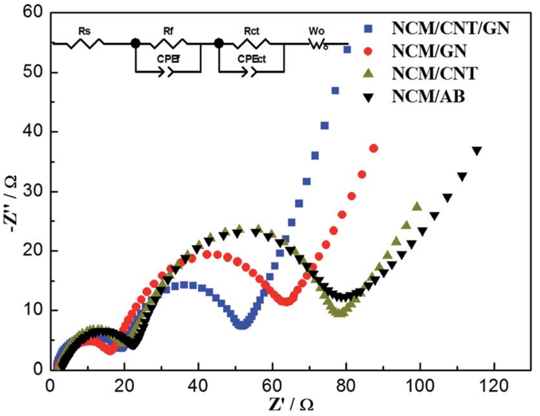

Fig. 9 Nyquist plots of NCM/CNT/GN, NCM/GN, NCM/CNT and NCM/AB electrodes after charge/discharge at 1.0C for 2 cycles. Inset is the equivalent circuit used for fitting the EIS spectra.

delivering higher charge and discharge specific capacities at different C rates than those of NCM/GN, NCM/CNT and NCM/AB.

Fig. 8 shows the cycling performances of NCM/CNT/GN, NCM/GN, NCM/CNT and NCM/AB electrodes at the current rate of 1.0C between 2.5 and 4.6 V. The NCM/CNT/GN hybrid material presents an initial discharge capacity of 162 mA h g^{-1}, and a discharge specific capacity of 152 mA h g^{-1} after 50 cycles, corresponding to a capacity retention of up to 93.8%. On the contrary, the NCM/GN, NCM/CNT and NCM/AB electrodes deliver initial discharge capacities of 152 mA h g^{-1}, 150 mA h g^{-1}, and 148 mA h g^{-1} at 1.0C, along with inferior capacity retention of 78.9%, 53.3% and 31.6%, respectively. Obviously, the NCM/CNT/GN electrode shows the best cycling performance among the samples, which should be attributed to the efficient increase of electronic conductivity in the presence of the 3D conductive network of CNT and GN. For the NCM/GN, NCM/CNT and NCM/AB electrodes, the relative poor cycling performances should be ascribed to the single GN, CNT or AB could not form efficiently conductive network in the electrode.

To further gain insight into the beneficial effect of 3D spider-web like electronic conducting network, the NCM/CNT/GN, NCM/GN, NCM/CNT and NCM/AB electrodes are investigated by EIS measurements. The impedance spectra in Fig. 9 were obtained after 2 cycles at 1.0C between 2.5 and 4.6 V. The impedance spectra were fitted with the equivalent circuit inset in Fig. 9 and the fitting results are listed in Table 3. The Nyquist plots of the electrodes can be distinguished in three parts, a small semicircle at high frequency region, a large semicircle at high-medium frequency region, and a slope line in low frequency region. The high-frequency semicircle is corresponding to the resistance of surface film (R_f) and the high-medium frequency semicircle is associated with the resistance of charge transfer (R_{ct}).[42] The slope line in low frequency region is related to the resistance of Li$^+$ ion diffusion through the solid electrode (W_o).[43] As showed in Fig. 9, the R_{ct} of NCM/CNT/GN electrode is much smaller than that of NCM/GN, NCM/CNT, or NCM/AB electrode. The smallest R_{ct} for NCM/CNT/GN electrode can be ascribed to the improvement of electrical conductivity at the assistance of 3D CNT/GN conductive network, which allows for prompt electron transport to enable the interfacial reactions during the lithium ion insertion and extraction processes. The relatively smaller of R_f for NCM/CNTs/GNs electrode are due to the wrapping of CNT/GN network, because the CNT/GN carbon matrix functions as a protecting layer and alleviates the unwanted side reactions between active material and the electrolyte.[44]

In addition, the lithium-ion diffusion coefficient was further calculated with the equation ($D = R^2T^2/2A^2n^4F^4c^2\sigma_w^2$), where σ_w^2

Table 3 Fitted results of the EIS spectra shown in Fig. 9

Samples	R_s/Ω	R_f/Ω	R_{ct}/Ω	σ_w	D (cm^2 s^{-1})
NCM/CNT/GN	1.86	18.33	36.49	11.97	1.04×10^{-10}
NCM/GN	2.05	19.23	55.97	14.01	7.62×10^{-11}
NCM/CNT	1.81	20.27	59.80	14.54	7.07×10^{-11}
NCM/AB	2.01	22.3	59.63	19.62	3.89×10^{-11}

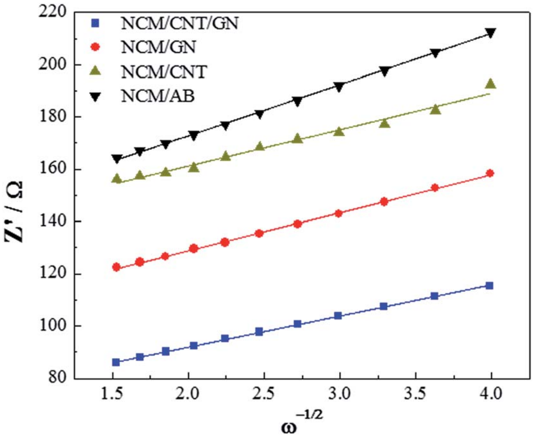

Fig. 10 Relationship between real resistance and frequency, the slope (Warburg impedance coefficient) of which was used to calculate the sodium-ion diffusion coefficient.

is the Warburg impedance coefficient, D is lithium-ion diffusion coefficient, R is the gas constant, T is the absolute temperature, A is the electrode area, n is the number of electron transferred per molecule during electrochemical reaction, F is Faraday constant, and c is molar concentration of Li^+.[45] The lithium-ion diffusion coefficients calculated using the above equation for the NCM/CNT/GN, NCM/GN, NCM/CNT and NCM/AB were 1.04×10^{-10} cm^2 s^{-1}, 7.62×10^{-11} cm^2 s^{-1}, 7.07×10^{-11} cm^2 s^{-1} and 3.89×10^{-11} cm^2 s^{-1}, respectively. It can be found that the NCM/CNT/GN shows the highest lithium-ion diffusion coefficient among the samples, which substantiates that the 3D spider-web like electronic conducting network is favorable for improving the lithium ion transportation inside the electrode (Fig. 10).

Conclusion

The influence of CNT + GN, GN, CNT and AB carbon conductive matrix on the electrochemical performance of $LiNi_{1/3}Co_{1/3}Mn_{1/3}O_2$ has been systematically investigated. In the structure of 3D spider web like conductive network design for the NCM/CNT/GN hybrid material, the NCM particles were well distributed among the graphene nanosheets, which alleviated the aggregation of GN. At the same time, the CNT supplied efficient linking between GN and the NCM particles, which could effectively construct a 3D electronic conducting network in the electrode of NCM/CNT/GN hybrid material. Such a unique 3D conducting network enables the fast electron and lithium ion transportation in the NCM/CNT/GN electrode, significantly ameliorating the interfacial reaction kinetics during battery cycling. As a result, the NCM/CNT/GN hybrid material exhibited the lowest electrode polarization as well as the superior rate capability and cycling performance in comparison with those of NCM/GN, NCM/CNT or NCM/AB hybrid material. The key findings of this work provide valuable clues for developing high performance cathode materials for lithium ion battery by constructing an efficient conducting network.

Acknowledgements

This work was carried out with financial support from the National Natural Science Foundation of China (grant no. 51474196, 51302232, 51502250), the Science & Technology Department of Sichuan Province (grant no. 2015JY0089, 2016RZ0071), and the project of Southwest Petroleum University (grant no. X151516KCL14).

References

1 A. Ritchie and W. Howard, *J. Power Sources*, 2006, **162**, 809–812.
2 S. Santhanagopalan, Q. Z. Guo, R. P. Ramadass and R. E. White, *J. Power Sources*, 2006, **156**, 620–628.
3 P. G. Balakrishnan, R. Ramesh and T. P. Kumar, *J. Power Sources*, 2006, **155**, 401–414.
4 R. V. Chebiam, A. M. Kannan, F. Prado and A. Manthiram, *Electrochem. Commun.*, 2001, **3**, 624–627.
5 C. Delmas, M. Ménétrier, L. Croguennec, I. Saadoune, A. Rougier, C. Pouillerie, G. Prado, M. Grüne and L. Fournès, *Electrochim. Acta*, 1999, **45**, 243–253.
6 A. Hirano, R. Kanno and Y. Kawamoto, *J. Solid State Chem.*, 1997, **134**, 1–4.
7 A. Rougier, I. Saadoune, P. Gravereau, P. Willmann and C. Delmas, *Solid State Ionics*, 1996, **90**, 83–90.
8 M. Yoshio, H. Noguch, J. Itoh, M. Okada and T. Mouri, *J. Power Sources*, 2000, **90**, 176–181.
9 C. S. Hua, K. Du, C. P. Tan, Z. D. Peng, Y. B. Cao and G. R. Hu, *J. Alloys Compd.*, 2014, **614**, 264–270.
10 T. Liu, S. X. Zhao, K. Z. Wang and C. W. Nan, *Electrochim. Acta*, 2012, **85**, 605–611.
11 X. Y. Han, Q. F. Meng, T. L. Sun and T. L. Sun, *J. Power Sources*, 2010, **195**, 3047–3052.
12 K. M. Shaju, G. V. Subba Rao and B. V. R. Chowdari, *Electrochim. Acta*, 2002, **48**, 145–151.
13 S. K. Hu, G. H. Cheng, M. Y. Cheng, B. J. Hwang and R. Santhanam, *J. Power Sources*, 2009, **188**, 564–569.
14 C. H. Lu and Y. K. Lin, *J. Power Sources*, 2009, **189**, 40–44.
15 H. B. Ren, Y. R. Wang, D. C. Li, L. H. Ren, Z. H. Peng and Y. H. Zhou, *J. Power Sources*, 2008, **178**, 439–444.
16 X. Z. Liu, H. Q. Li, E. Yoo, M. Ishida and H. S. Zhou, *Electrochim. Acta*, 2012, **83**, 253–258.
17 K. Araki, N. Taguchi, H. Sakaebe, K. Tatsumi and Z. Ogumi, *J. Power Sources*, 2014, **269**, 236–243.
18 J. Cho, Y. W. Kim, B. Kim, J. G. Lee and B. Park, *Angew. Chem., Int. Ed.*, 2003, **42**, 1618–1621.
19 Y. H. Ding, P. Zhang, Z. L. Long, Y. Jiang and F. Xu, *J. Alloys Compd.*, 2009, **487**, 507–510.
20 S. K. Hu, T. C. Chou, B. J. Hwang and G. Ceder, *J. Power Sources*, 2006, **160**, 1287–1293.
21 D. T. Liu, Z. X. Wang and L. Q. Chen, *Electrochim. Acta*, 2006, **51**, 4199–4203.
22 Y. S. He, L. Pei, X. Z. Liao and Z. F. Ma, *J. Fluorine Chem.*, 2007, **128**, 139–143.
23 G. Y. Li, Z. L. Huang, Z. C. Zuo, Z. J. Zhang and H. H. Zhou, *J. Power Sources*, 2015, **281**, 69–76.
24 N. N. Sinha and N. Munichandraiah, *J. Am. Chem. Soc.*, 2009, **1**, 1241–1249.
25 R. Guo, P. F. Shi, X. Q. Cheng and C. Y. Du, *J. Alloys Compd.*, 2009, **473**, 53–59.
26 Q. T. Zhang, G. C. Peng, G. P. Wang, M. Z. Qu and Z. L. Yu, *Solid State Ionics*, 2009, **180**, 698–702.
27 G. P. Wang, Q. T. Zhang, Z. L. Yu and M. Z. Qu, *Solid State Ionics*, 2008, **179**, 263–268.
28 G. X. Wang, M. Z. Qu, Z. L. Yu and R. Z. Yuan, *Mater. Chem. Phys.*, 2007, **105**, 169–174.
29 A. Varzi, C. Täubert and M. W. Mehrens, *Electrochim. Acta*, 2012, **78**, 17–26.
30 S. S. Jan, S. Nurgul, X. Q. Shi, H. Xia and H. Pang, *Electrochim. Acta*, 2014, **149**, 86–93.
31 J. W. Lee, J. H. Lee, T. T. Viet, J. Y. Lee, J. S. Kim and C. H. Lee, *Electrochim. Acta*, 2010, **55**, 3015–3021.
32 X. Y. Zhang, A. Mauger, Q. Lu, H. Groult, L. Perrigaud, F. Gendron and C. M. Julien, *Electrochim. Acta*, 2010, **55**, 6440–6449.

33 H. Porthault, R. Baddour-Hadjean, F. Le Cras, C. Bourbon and S. Franger, *Vib. Spectrosc.*, 2012, **62**, 152–158.

34 J. J. Li, H. Q. An, J. Zhu and J. W. Zhao, *Sens. Actuators, B*, 2016, **235**, 663–669.

35 S. S. Nanda, M. J. Kim, K. S. Yeom, S. S. A. An, H. Ju and D. K. Yi, *TrAC, Trends Anal. Chem.*, 2016, **80**, 125–131.

36 L. Li, J. C. Xu, G. H. Li, X. L. Jia, Y. F. Li, F. Yang, L. Q. Zhang, C. M. Xu, J. S. Gao, Y. Liu and Z. W. Fang, *Chem. Eng. J.*, 2016, **284**, 78–84.

37 S. Ghosh, K. Ganesan, S. R. Polaki, T. Mathews, S. Dhara, M. Kamruddin and A. K. Tyagi, *Appl. Surf. Sci.*, 2015, **349**, 576–581.

38 K. M. Shaju, G. V. S. Rao and B. V. R. Chowdari, *Electrochim. Acta*, 2002, **48**, 145–151.

39 Z. D. Huang, X. M. Liu, S. W. Oh, B. Zhang, P. C. Ma and J. K. Kim, *J. Mater. Chem. A*, 2011, **21**, 10777–10784.

40 X. Z. Liu, H. Q. Li, D. Li, M. Ishida and H. S. Zhou, *J. Power Sources*, 2013, **243**, 374–380.

41 F. X. Wang, Y. Liu, X. W. Wang, Z. Chang, Y. P. Wu and R. Holze, *ChemElectroChem*, 2015, **2**, 1024–1030.

42 X. Y. Qiu, Q. C. Zhuang, Q. Q. Zhang, R. Cao, Y. H. Qiang, P. Z. Ying and S. G. Sun, *J. Electroanal. Chem.*, 2013, **688**, 393–402.

43 J. H. Park, J. H. Cho, S. B. Kim, W. S. Kim and S. Y. Lee, *J. Mater. Chem.*, 2012, **22**, 12574–12581.

44 X. Li, J. Xu, P. X. Huang, W. Yang, Z. Q. Wang, M. S. Wang, Y. Huang, Y. Zhou, M. Z. Qu, Z. L. Yu and Y. H. Lin, *Electrochim. Acta*, 2016, **190**, 69–75.

45 J. M. Zheng, P. F. Yan, W. H. Kan, C. M. Wang and A. Manthiram, *J. Electrochem. Soc.*, 2016, **163**(3), A584–A591.